Energy Storage Concentrates on Solar Air Heaters with Artificial S-shaped Irregularity on the Absorber Plate

Mostafa Esmaeili Shayan*[1] , Farzaneh Ghasemzadeh[2], Seyed Hossein Rouhani[3]

[1] *Department of Biosystem Engineering(), Tarbiat Modares University, Tehran, Iran, E.mostafa@modares.ac.ir*

[2] *Department of Physics, Iran University of Science and Technology, Tehran, Iran, f_ghasemzadeh@physics.iust.ac.ir*

[3] *Department of Electrical Engineering, National Kaohsiung University of Science and Technology, Kaohsiung, Taiwan, hosseinrouhani@nkust.edu.tw*

**Corresponding Author: E.mostafa@modares.ac.ir*

Abstract: This study utilizes the friction factor as a means to evaluate the impact of the roughness parameter on both heat transfer and pressure drop. This work involves doing an experimental and numerical investigation on the utilization of artificial roughness in solar air heaters situated in outdoor settings. The study examines the effects of using a rectangular S-shaped arrangement of artificial roughness, both in an inline and staggered configuration. The objective of this study is to validate the enhanced thermo-hydraulic performance of solar air heaters using various arrangements of artificial roughness shapes. The parameters considered include the length of the relative roughness (d/H = 1.33), the height of the relative roughness (e/H = 0.271), and the constant distance between S (b/H = 0.667). The Reynolds number is varied within the range of 3000 to 10000, while the pitch range (p/H) is set to (1.667, 3.33, 5,6.667) for in-line arrangements and (l/H) is set to (0.8335, 1.666, 2.5, and 3.335) for staggered arrangements. The results show that enhancing heat transfer using an artificial roughness staggered arrangement is the best. The maximum Nusselt number was observed at a dimensionless pitch-to-height ratio of 3.33 for both inline and staggered arrangements, with values of 4.87 and 4.2 times higher than that of the smooth duct, respectively.

Keywords: Heat Transfer, Solar Air Heaters, Artificial Roughness, Thermo-Hydraulic Performance, Nusselt Number.

Nomenclature			
Symbols		**Subscript**	
α	Angle of Attack	ε	Constants
ρ	Density	*deg*	Degree

W/H	Duct Aspect Ratio	*h*	Hydraulic
D_h	Duct Hydraulic Diameter	∇	Impact of Each Parameter
f	Friction Factor	*r*	Relative
Q	Heat	*s*	Smooth
Ng	Number of Main Gaps	*t*	Time
Nu	Nusselt Number	**Acronyms**	
g/e	Ratio of Gap Width to Rib Height	*CFD*	Computational Fluid Dynamics
P′/P	Ratio of Staggered Rib Position to Pitch	*DPSAH-CMA*	Double Pass Solar Air Heater with a Cross-Matrix Absorber
r/e	Ratio of Staggered Size to Rib Height	*GI*	Galvanized Iron
g′/e	Relative Gap Size of Additional Gap in Symmetrical Rib Elements	*GCP*	Granular Carbon Powder
e/Dh	Relative Roughness Height	*HT*	Heat Transfer
p/H	Relative Roughness Pitch	*THIP*	Maximal Thermo Hydraulic Improvement Parameter
Re	Reynolds Number	*PCMs*	Phase Change Materials
C_p	Specific Heat	*RF-SAH*	Return Flow Solar Air Heater
T	Temperature	*Re*	Reynolds Number
K	Thermal Conductivity	*SRVG*	Silastic Ring Vertical Gastroplasty
G_k	Turbulence Kinetic Energy	*SAH*	Solar Air Heaters
v	Velocity	*TPF*	Thermal Performance Factor
μ	Viscosity	*THPP*	Thermo Hydraulic Performance Parameter

1. Introduction

Considering the growing demands of modern societies and sustaining industrial and economic growth, energy plays an increasingly important role. The International Energy Outlook, according to Enhancing energy intake from renewable energy sources and developing energy storage technologies can reduce the unpredictability and increase the use of these sources [1]. As the world population continues to increase and the availability of fossil fuels begins to dwindle, it may no longer be viable to meet the global energy demand solely through the use of fossil fuels. The rapid depletion and increasing unpredictability of fossil fuel prices have driven the advancement of renewable energy sources as reliable alternatives for meeting our energy needs. In terms of renewable energy, solar energy has the advantage of being easily accessible and implemented. [2].

Solar air collectors heat air using solar energy, which is its main environmental benefit. Solar appliances are environmentally and health-friendly. Today's energy consumers favour solar energy goods and solutions. Solar air collectors directly heat air without electricity. Hence, solar air warmers may minimise ecosystem carbon emissions [3]. Solar energy stands out as a sustainable, abundant, and environmentally friendly renewable resource, surpassing other alternative energy sources due to its ethical production methods and minimal impact on the environment [4]. In the long term, renewable energy holds the potential to replace a substantial amount of conventional power. A solar air heater (SAH) is a specialized device that is engineered to capture incident solar radiation and convert it into usable thermal energy for a wide range of practical purposes [5]. One efficient method for enhancing the rate of heat transfer in a SAH is to employ artificial roughness geometry on the absorber plate (AP) [6]. Researchers conducted experiments with different roughness geometries for duct performance optimization. Their objective was to achieve the optimal balance between the improved performance of the increased pump power required to maintain airflow.

Within the field of surface aerodynamics and hydrodynamics studies, researchers have undertaken investigations pertaining to the amalgamation of two distinct roughness geometries [5,7]. The year 2022 witnessed the experimental evaluation of a thermal energy storage material within the tube of a double-pass solar air heater (DPSAH) that was equipped with a cross-matrix absorber (CMA). DPSAH-CMA with Phase Change Materials (PCMs) showed the highest storage effectiveness at higher mass flow rates (MFRs), which was directly proportional to solar radiation levels. DPSAH-CMA-with PCM has 17% greater thermal efficiency than DPSAH-CMA-without PCM in outdoor circumstances. The energy efficiency of the DPSAH-CMA system with phase change material (PCM) was measured to be 23%, whereas the energy efficiency of the DPSAH-CMA system without PCM was found to be 15%. The DPSAH-CMA-with PCM system has a cost-benefit ratio of 0.17 RM/kWhr, which is 22% lower than alternative systems [8]. A new SAH incorporating the PCM was developed in 2023. The average percentage variation between the actual and projected outlet temperatures for three phase change materials is found to be 4.50% for paraffin wax, 2.63% for acetamide, and 2.32% for stearic acid.

A SAH without PCM was compared to one equipped with stearic acid, acetamide, and paraffin wax during charging and discharging. The SAHs with PCM demonstrated a 15.09% higher efficiency compared to the those without PCM. In particular, the use of paraffin wax in the solid-liquid phase change material showed an increase of 8.18% in the specific absorption rate, whilst the utilization of acetamide resulted in a 6.67% improvement compared to the SAR without PCM [9]. A study was conducted in 2022 to examine the flow characteristics of fluids passing through a heat exchanger with bench-fin configuration in an apartment setting, with the inclusion of vortex generators. By employing a numerical technique, the researchers successfully achieved a faithful reproduction of the local Nusselt number distribution characteristics in the given geometry [7]. In order to improve the efficiency of heat conduction, a range of geometries are employed, which may involve the utilization of either a singular form of roughness or a mixture of two distinct types of roughness elements [6]. The SAH is a one-of-a-kind heat exchanger that generates thermal energy for residential heating, greenhouses, the drying of agricultural products, certain industrial applications, and places where conventional energy sources are necessary [10].

The development of the SAH device aimed at energy storage through the use of a series of five evacuated tubes, along with the incorporation of storage materials. The innovative SAH gadget examines heat transport and extends system operation. The device outlet temperatures were measured at 110 °C and 118 °C when operating at a mass flow rate of 0.006 kg/s, both with and without the presence of storage materials. These measurements were taken at different airflow rates. Charged storage materials reach 95 °C. With and without storage material, thermal efficiency achieved 64.23 and 31.02 % at 0.05 kg/s airflow. Maximum usable power reaches 3190 and 2836 W [11]. Also, in a research study, the researchers analyzed the impact of using a curved shape in a SAH by employing mathematical and computer modeling. They reported a positive effect of utilizing a curved shape [12]. Increasing the roughness level or using curved lines has a positive effect on the thermohydraulic variable [13]. Solar collectors are capable of converting the sun's irradiance into the water- or air-heating heat. SAHs have found application in a wide range of energy-saving scenarios, especially where a low to moderate air temperature is needed. SAHs offer advantages by eliminating risks associated with leaks, freezing or stagnation, and environmental or health hazards. However, the limited heat-carrying capacity of air restricts their use in high-temperature operations, impacting the efficiency of solar heaters. To address this limitation, researchers have been exploring innovative methods to enhance SAH performance and reduce efficiency drops during high-temperature operations [14]. A redesigned v-corrugated AP is tested to improve the SAH collector performance. The modified and standard v-corrugated collectors with jet plate blown systems are evaluated for thermal efficiency. Model-1 is the modified system and Model-2 the conventional system. Model-1's increased thermal efficiency shows that the updated model improves heat exchange efficiency [15]. One of the most commonly recommended techniques for increasing passive HT and improving the thermal effectiveness of SAHs is artificial roughness on the AP [3]. One of the widely recognized techniques involves the placement of impediments within the flow stream on the absorbent plate. They are diverse as obstacles in the form of rib[16,17], fins[18,19], baffles[20,21], ailerons[22–24]. A SAH comprising a PCM block heat storage unit was tested in Eastern Morocco under real-world climatic conditions. The examination involved utilizing computational fluid dynamics (CFD) along with a C++ code that incorporated user-defined function types. This work optimised the SAH for apricot drying conditions. SAHs without PCM rise beyond 70 °C, which might degrade product quality. A tilt of 60° has been found to have a positive impact on the mass flow rate of natural convection, resulting in an increase in the output temperature of the solar air heater and a faster melting process of the phase change material. The drying chamber investigated these ideal scenarios. Forced convection improved air homogeneity and temperature [25].

In a study, AP undersides had three-arc rib roughness. The study thoroughly examines the performance of a single glazed duct solar air heater under conditions of steady flow. The study focuses on several roughness components, such as the number of gaps (ranging from 1 up to 3), The relative gap width ranges from 0.5 to 1.5, whereas the relative gap position ranges from 0.3 to 0.9. This comprehensive examination aims to gain valuable insights into the impact of these roughness elements on the SAH 's efficiency. The Nusselt number (Nu) and friction factor (f) have a quadratic association that is generally applicable, with percentage variations from experimental values of around 6.15% and 5.74%, respectively. The optimal thermal hydraulic performance, with a relative gap width of 1, gap location at 0.6, and three gaps, is determined to be 3.85 [26]. In Moradabad, India, a study was conducted to test modified SAHs equipped with PCMs under the local climate conditions. The thermal performance metrics of these redesigned systems were evaluated for different MFRs (0.01, 0.02, and 0.03 kg/s) and PCM masses. The SAH with PCM-filled miniature cylindrical tubes exhibited a notable enhancement as compared to the SAH with a flat absorber plate under conditions of forced convection. It achieved a maximal temperature differential between exhaust air and ambient air ranging from 2 to 9 °C. Among the configurations tested, Configuration 4 was identified as the most effective for room heating and agricultural drying purposes. It achieved an exhaust temperature of 48°C for at least 9.8 hours per day, resulting in a daily efficiency of 66%. This configuration showed promising results for enhancing energy utilization in heating and drying applications [27]. The comprehensive experimental analysis included the examination of several parameters, such as the aspect ratio (W/H) of the duct, which was set at 12. The relative roughness height (e/Dh) was determined to be 0.043, while the relative roughness pitch (p/H) was set at 10. The angle of attack (α) was established at 60 degrees. Additionally, the ratio of gap width to rib height (g/e) was determined to be 4, and the ratio of staggered rib position to pitch (P'/P) was set at 0.4. The ratio of staggered size to rib height (r/e) was established at 4. Furthermore, the relative gap size of an additional gap in symmetrical rib elements (g'/e) was varied between 0.5 and 2. Finally, the number of main gaps (Ng) was set at 4. The suggested roughness geometry was compared to prior geometry, and it showed remarkable results. The results indicate that the maximum increase in f and Nu was found to be 2.70 and 2.51 times higher, respectively, compared to a flat plate, under the conditions where the ratio of the groove height to the equivalent roughness height (g'/e) was 1 and the ratio of the groove depth to the groove width (d/w) was 0.65. The thermal hydraulic performance (THP) reached 1.82 under the same conditions (d/w = 0.65 and g'/e = 1). These findings indicate significant improvements in HT and flow resistance compared to previous geometry configurations [28]. The researcher concentrated on a practical experiment with an artificially roughened SAH [29]. The Baffles 90° models were used to determine the optimal baffle position. After testing, it was found that positioning the baffles in the center of the second model with 18 bars resulted in an efficiency of 85%. SAH-A and SAH-B were investigated using paraffin wax as an inexpensive energy storage medium. The transformation of SAH-B into SAH-C has been achieved by employing a precise combination of granular carbon powder (GCP) and paraffin wax. SAH-C outperforms both SAH-B and SAH-A. SAH-C has a thermal efficiency of 79.10%, while SAH-B and SAH-A have thermal efficiencies of 50% and 57.41%, respectively. The heat transfer coefficient for SAH-A is measured to be 249.19 W/m²K, while SAH-B exhibits a coefficient of 389 W/m²K, and SAH-C has a coefficient of 411.05 W/m²K. The upper limit of the exhaust temperature for SAH-C is recorded at 52.5°C, while SAH-B's is 46.9°C and SAH-44.7's is 44.7°C. The major qualities of SAH-C demonstrate its cost-effectiveness and efficiency as a model for many applications such as space heating, drying, and lumber seasoning. The best-configured SAH-C models cost $67 [30]. A SAH composed of three air flow ducts was investigated by Singh and Dhiman in 2018, with total MFR proportions incorporated into the first and second ducts. Two scenarios were examined to assess the impact of fractional total MFR: (i) two streams with equal MFR fractions, and (ii) unequal MFR fractions passing by the first and second ducts of the SAH. In comparison to another type of recirculating heater with equivalent geometric and operational flow conditions, the suggested SAH demonstrated notably higher thermo-hydraulic efficiency. This was achieved with a lower recycling ratio and an equal proportion of the total MFR. The findings suggest the superiority of the proposed SAH regarding performance and efficiency compared to the alternative recirculating heater [31]. A return flow SAH (RF-SAH) with V-type artificial assimilation was simulated and numerically studied to validate the study's results. Several researchers have made improvements to the baffles used in the RF-SAH. The research examines the thermo-hydraulic, thermal, and baffle effectiveness parameters of the RF-SAH. According to the study, using RF-SAH with baffles on both sides of the AP and a MFR greater than 0.2 kg/s maximizes both thermal and thermo-hydraulic efficiency. The numerical model utilized in the study accurately matches experimental findings, with an average error rate of 16.45%. Baffles positioned below, above, and on both sides of the AP are found to maximize the thermal and thermo-hydraulic effectiveness of RF-SAH. In comparison, RF-SAH outperforms Single-Flow SAHs (SF-SAH) in terms of thermal efficiency.The inclusion of ideal baffle roughness improves air retention time, leading to a more efficient output. Overall, the study highlights the potential of RF-SAH with properly designed baffles to enhance thermo-hydraulic, and thermal performance, making it a promising technology for solar air heating applications [32].

As mentioned in the literature review, the arrangement of roughness elements on the AP has a profound effect on secondary flow development within the flow passage. The formation of secondary flow over the airfoil profile can be significantly influenced by even a little modification in the arrangement of roughness features. This underscores the importance of carefully designing the roughness element pattern to optimize the flow characteristics and improve the overall SAH performance. The main aim of this study is to examine the factors that contribute to attaining maximum heat transfer and thermal efficiency in a solar air heater through the implementation of a rectangular S-shaped artificial roughness pattern on the absorber plate. The study introduces a novel roughness element pattern that combines curvature and increased roughness, which has not been utilized by other researchers, highlighting the originality of the current investigation. The primary objective of this study is to evaluate the influence of the roughness pattern on the thermal performance and flow properties of the SAH. Additionally, the study aims to derive correlations for the *Nu* and *f*, providing valuable insights into the flow behavior and HT within the SAH equipped with the novel roughness pattern.

2. Experimental Apparatus

2.1. Experimental process:

The experiment was conducted in Tehran, Iran at an elevation of 900 meters. The average weather during the experiment was 31 °C, with winds blowing at 23 km/h from the south and humidity at 11%. The experiment was conducted at coordinates 35.7219°N, 51.3347°E in the year 2022. Day length and number of sunny hours are optimal in Tehran. In high-latitude locations, peak sunshine hours regularly exceed 9 hours per day. It can be shown that Iran, with 300 sunny days per year, has one of the highest potentials for solar energy among all countries. Values for all constant parameters are as follows: solar intensity ranges from 100-900 W/m, and the absorptivity of the cover is 0.05. The transmissivity of the solar air heater cover is measured to be 0.8. Additionally, the absorptivity of the absorber plate of the SAH is determined to be 0.96, while the emissivity of the cover is found to be 0.94. Fig.1 depicts the experimental configuration of the SAH system. The experimental apparatus consists of a rectangular duct constructed of galvanized iron and an insulating layer of glass wool is used to prevent heat loss to the outside air. The duct has a thickness of 4 cm and a cross-sectional area of 300 mm x 30 mm. To generate turbulent flow, the aspect ratio (W/H) of two channels in the SAH is maintained at 10. The ASHRAE standard for thermal solar collectors mandates that the minimum dimensions for the inlet and outlet be determined using mathematical formulas. Specifically, the inlet dimensions should be calculated as 5 times the square root of the product of the width (W) and height (H), while the outlet dimensions should be calculated as 2.5 times the square root of the product of the width (W) and height (H) ($5\sqrt{WH} \times 2.5\sqrt{WH}$). Figure 1 shows the schematic of the Solar Air Heater device. A centrifugal blower propels the air, controlled by a valve. A calibrated vane-type anemometer (AM-4206M) is employed to measure the velocity of exiting air. The sun irradiance was measured using a TM-207 calibrated solar power meter, which has an accuracy of 5% and a range of 0-2000 W/m2. The test section includes a 1 mm thick aluminum AP with dimensions of 1200 mm x 300 mm. Six K-type thermocouples are utilized to monitor the outlet and input temperatures, along with the temperature of the absorbent plate, for each of the two devices. Using a data logger, all temperature values from the monitoring equipment were reliably recorded. A digital manometer measures the pressure difference between the test portions with 5% accuracy in kPa. Table 1 contains the physical characteristics of single-pass SAH.

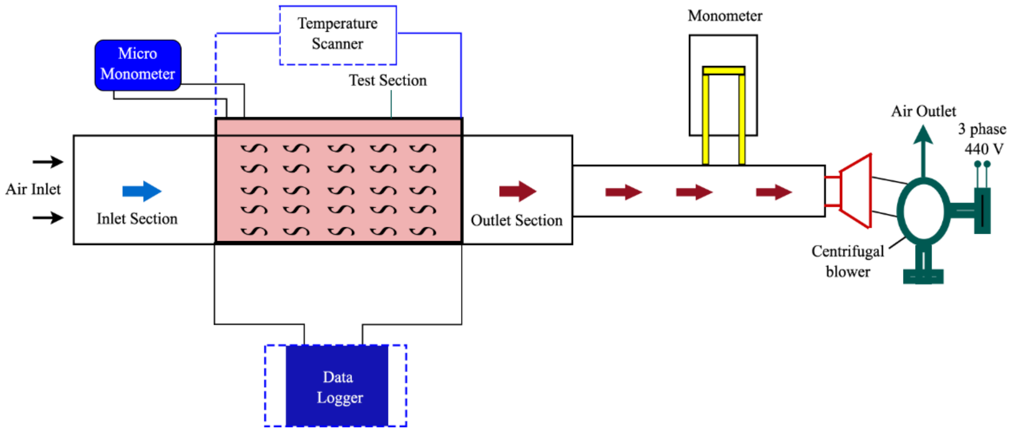

Figure 1. Schematic of Solar Air Heater device.

2.2. Rectangular stripe artificial roughness:

The Fig. 2 representation of artificial roughness for a rectangular stripe with an S-shaped geometry is lined and staggered. Each rectangular stripe is 0.5 mm thick and constructed from galvanized iron (GI). A particle measuring 1.2 cm in height and 4 cm in width was placed on an AP with different pitch ranges. For the silastic ring vertical gastroplasty (SRVG) in line, the pitch range was (p/H) = (1.667, 3.33, 5, 6.667), while for staggered, it was (l/H) = (0.8335, 1.666, 2.5, and 3.335). The α was set at 60°

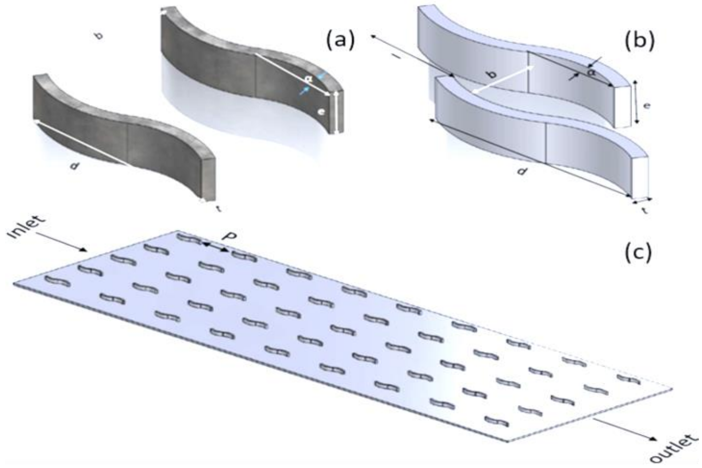

Figure 2. Schematic view of (a) rectangular S-shape inline, (b) rectangular S-shape staggered (c) AP with artificial roughness.

Table 1. Specification of SAH with artificial roughness units in the experimental rig.

Parameters	Value
Entrance length of the duct (L_1)	600 mm
Testing duct length (L_2)	1200 mm
Exit channel length (L_3)	300 mm
Duct size (W)	300 mm
Length of the conduit (H)	30 mm
Duct hydraulic diameter (D_h)	54 mm
Rib height (e)	10.2 mm
Pitch (P)	5,10, 15 and 20 cm
Aspect ratio (W/H)	10

3. Experimental Analysis

After 50 minutes, the temperature of the fluid or absorbent plate has not changed, we can conclude that a steady state has been reached. The dimensionless results of the experiment are expressed through the *f*, *Nu*, and thermal enhancement coefficients. HT is determined by assuming that heat loss equals HT in a steady state. From equations (1), (2), and (3) [33].

$$Q_{air} = Q_{loss} \tag{1}$$

$$where: Q_{air} = \dot{m}C_{p,air}(T_{out} - T_{in}) \tag{2}$$

The test part's convective HT may be expressed as follows:

$$Q_{loss} = hA\left(\tilde{T}_{ap} - T_{am}\right) \tag{3}$$

In which [34]

$$T_{am} = \frac{(T_{out}+T_{in})}{2} \tag{4}$$

And the temperature of the AP [34]

$$\tilde{T}_{ap} = \sum T_{ap}/12 \tag{5}$$

The average HT coefficient that was used from experimental data and after that calculation Nu from the following expression [35]:

$$h = \frac{\dot{m}C_{p,air}(T_{out}-T_{in})}{A(T_{ap}-T_{am})} \tag{6}$$

Therefore, the *Nu* and Re were calculated using the following equations [36,37]:

$$Nu = \frac{hD_h}{k} \tag{7}$$

$$Re = \frac{\rho v \, D_h}{\mu} \tag{8}$$

Friction factor that calculated pressure drop given by [35]:

$$f = \frac{2}{L/D_h}\frac{\Delta P}{\rho v^2} \tag{9}$$

Thermal enhancement factor that expression relative to the smooth duct given by [38]:

$$TPF = \frac{\left({}^{Nu_r}/_{Nu_s}\right)}{\left({}^{f_r}/_{f_s}\right)^{\frac{1}{3}}} \tag{10}$$

4. Describe the CFD Model

This study examines the impact of artificial roughness on the thermal performance and heat transfer of a single-pass solar air heater.

4.1 Geometry Creation

The model is created in SolidWorks 2019 and exported to Ansys Fluent 17.0 to simulate a solar heater with a smooth channel and artificially added roughness. By utilizing the same measurements as in the practical experiment, the model depicted in Table 1 is developed according to the schematic presented in Figure 3.

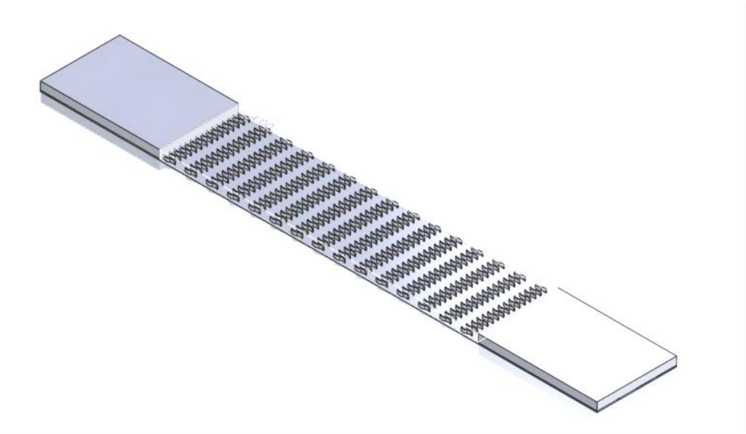

Figure 3. Geometry created by the CAD program

4.2 Mesh Generation

The model's mesh is visible in Figure 4. It depicts the domain as a network of triangular cells. The main objective of mesh generation in finite element method is to subdivide a domain into smaller subdomains. SAH module is meshed in Fluent utilizing the physics-controlled mesh sequence option to ensure precise resolution of the HT and flow fields. As shown in Table 2, we utilized free tetrahedral and free triangular mesh settings to generate all of the models.

Table 2. Statistic of mesh generation

No.	Number of Nodes	Number of elements
1	2,800,989	8,673,036

Figure 4. MESH representation with triangle cell for S-shaped artificial roughness and structure mesh dominant.

4.3 Governing Equations

The equations for momentum, continuity, and energy in three dimensions are derived based on the assumptions established in the study [39]

1. Continuity Equation (Conservation of Mass):

$$\frac{\partial u_s}{\partial x}+\frac{\partial v_s}{\partial y}+\frac{\partial w_s}{\partial z}=0 \qquad (11)$$

2. momentum equation

- in x-direction

$$\rho\left(u_s\frac{\partial u_s}{\partial x}+v_s\frac{\partial u_s}{\partial y}+w_s\frac{\partial u_s}{\partial z}\right)=-\frac{\partial p}{\partial x}+\frac{\partial}{\partial x}\left(\mu\frac{\partial u_s}{\partial x}\right)+\frac{\partial}{\partial y}\left(\mu\frac{\partial u_s}{\partial y}\right)+\frac{\partial}{\partial z}\left(\mu\frac{\partial u_s}{\partial z}\right) \qquad (12)$$

- in y- direction

$$\rho\left(u_s\frac{\partial v_s}{\partial x}+v_s\frac{\partial v_s}{\partial y}+w_s\frac{\partial v_s}{\partial z}\right)=-\frac{\partial p}{\partial y}+\frac{\partial}{\partial x}\left(\mu\frac{\partial v_s}{\partial x}\right)+\frac{\partial}{\partial y}\left(\mu\frac{\partial v_s}{\partial y}\right)+\frac{\partial}{\partial z}\left(\mu\frac{\partial v_s}{\partial y}\right) \qquad (13)$$

- in z-direction

$$\rho\left(u_s\frac{\partial w_s}{\partial x}+v_s\frac{\partial w_s}{\partial y}+w_s\frac{\partial w_s}{\partial z}\right)=-\frac{\partial p}{\partial x}+\frac{\partial}{\partial x}\left(\mu\frac{\partial w_s}{\partial x}\right)+\frac{\partial}{\partial y}\left(\mu\frac{\partial w_s}{\partial y}\right)+\frac{\partial}{\partial z}\left(\mu\frac{\partial w_s}{\partial z}\right) \qquad (14)$$

3. Equation of energy:

$$\frac{\partial T}{\partial t}+u_s\frac{\partial T}{\partial x}=\alpha\frac{\partial^2 T}{\partial x^2} \qquad (15)$$

4. Transport equation for the RNG k-ε model [40-41]

$$\frac{\partial(\rho k)}{\partial t}+\frac{\partial(\rho u_s k)}{\partial x}=-\frac{\partial}{\partial t}\left[\left(a_k\mu_{eff}\right)\frac{\partial k}{\partial x}\right]+G_k+G_b-\rho\varepsilon-Y_M+S_k \qquad (16)$$

$$\frac{\partial(\rho k)}{\partial t}+\frac{\partial(\rho u\varepsilon)}{\partial x}=-\frac{\partial}{\partial t}\left[\left(a_k\mu_{eff}\right)\frac{\partial \varepsilon}{\partial x}\right]+G_{1\varepsilon}\frac{\varepsilon}{k}\left(G_k+G_{3\varepsilon}G_b\right)+G_{2\varepsilon}\rho\frac{\varepsilon^2}{k}-R_\varepsilon+S_k \qquad (17)$$

In the given equation, the terms denoted as G_k represent the generation of turbulence kinetic energy resulting from the mean velocity gradient and buoyancy, respectively and $G_{1\varepsilon}=0.09, G_{3\varepsilon}=1.92$, and $G_{2\varepsilon}=1.44$ that constant respectively [42].

4.4 Boundary condition

In general, the computational domain comprises a SAH duct with an AP sitting on the x-y-z plane, surrounded by the intake, outlet, and both upper and lower wall boundaries. As the equation momentums are solved in the arithmetic domain, the terms of the non-slip boundary on the airway walls are assumed throughout the whole state. The lower wall of the SAH is thermally insulated, meaning it is adiabatic. In contrast, the upper wall of the SAH is exposed to average solar radiation throughout the day, resulting in a constant heat flux of 965 W/m2. It is assumed that the temperature of the air within the duct remains constant at 300 K. In the case of the input limitations of the arithmetic range, a variable air flow rate with velocity values of (0,9, 1,5, 2, and 2.5 m/ s) is provided. At flow inlets, MFR inlet boundary conditions are often employed to determine flow velocity and all related numerical flow parameters. In this simulation, four uniform MFRs are established at the field's entrance. The Re is employed to determine the velocity of the flow intake. On leaving the arithmetic domain, the port boundary condition is given. At the output of the outlet, continuous pressure of 1.013 x 10^5 Pa is applied to the outlet boundary condition. The thermo-physical parameters of air, aluminum absorption plate, and galvanized iron are displayed in Table 3.

Table 3. Thermophysical Properties of the Material for Experimental Rig and Numerical Simulation

Properties	**Air**	**Aluminum**	**GI**	**Glass**
Density (ρ)	1.225 kg/m^3	2719 kg/m^3	7870 kg/m^3	2600 kg/m^3
Specific heat (C_p)	1006.4 j/kg k	871 j/kg k	896 j/kg k	840 j/kg k
Viscosity(μ)	1.789e-05 kg/m-s	-	-	-
Thermal conductivity (K)	0.0242 w/m^2-k	202.4 W/m^2-k	204.2 W/m^2-k	1.05 W/m^2-k

5. Results and Discussion

To verify the *Nu* for the smooth SAH, the correlation equation from Dittus-Boelter was employed [43], as:

$$Nu = 0.023Re^{0.8}Pr^{0.4} \qquad (18)$$

Gnielinski Equation given by [43]:

$$Nu = \frac{\left(\frac{f}{8}\right)(Re-1000)Pr}{1+12.7\left(\frac{f}{8}\right)^{\frac{1}{2}}\left((pr)^{\frac{2}{3}}-1\right)} \;;\; for\ 3000 < Re < 5\times10^6 \qquad (19)$$

To valid *f* for the smooth SAH, the correlation equation from the Blasius was employed [43], as:

$$f = 0.316Re^{-0.25} \qquad , for\ 3000 \le R \le 20000 \qquad (20)$$

Petukov Equation given by [43]:

$$f = (0.79\times\ln Re - 1.64)^{-2} \qquad , for\ 3000 < Re < 5\times10^6 \qquad (21)$$

Figures 5 and 6 illustrate the connection between the f and Nu parameters with respect to the Re variable for the smooth SAH in both the present study and previously established correlation equations. The data obtained in the current study aligns well with the findings of prior correlation equations, indicating a significant level of concurrence.

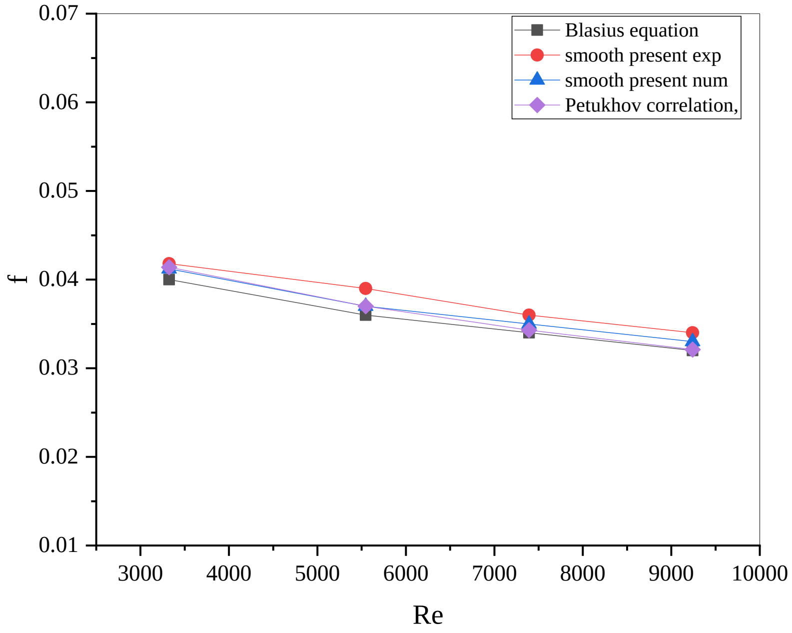

Figure 5. Validation of *f* for the smooth SAH with the correlation equation from the Blasius.

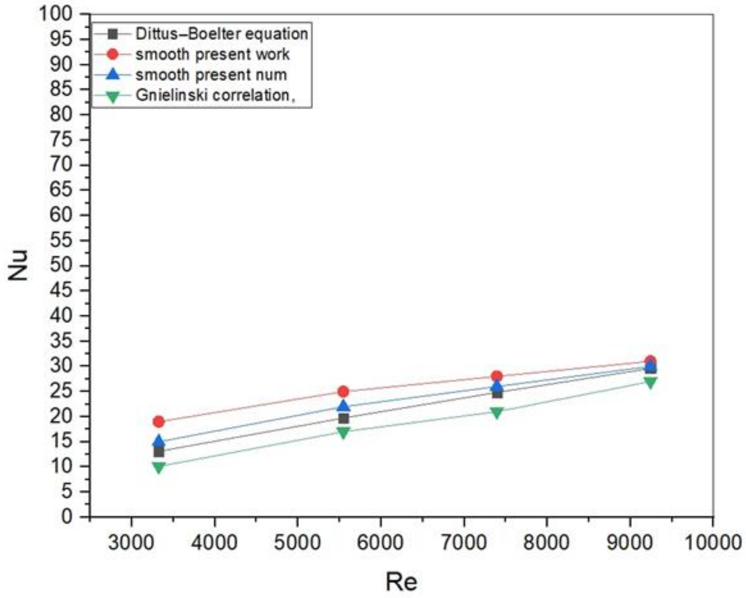

Figure 6. ***Nu* validation for the smooth SAH using the Dittus-Boelter correlation equation.**

5.1 Effect of arrangement of S-shape artificial roughness on HT

Figure 7 illustrates the temperature and velocity contours along the solar heater using an S-shaped roughness with inline and staggered arrangements at a Re of 7393 and α=60°, with (d/H = 1.33, e/H = 0.271, and b/H = 0.667). This figure illustrates an S-shaped distribution of velocity and temperature for the SAH. The numerical analysis shows how the incorporation of synthetic roughness, which is embedded and overlapping, affects the velocity and temperature of the SAH. With its S-shaped roughness, heat transport will be improved.

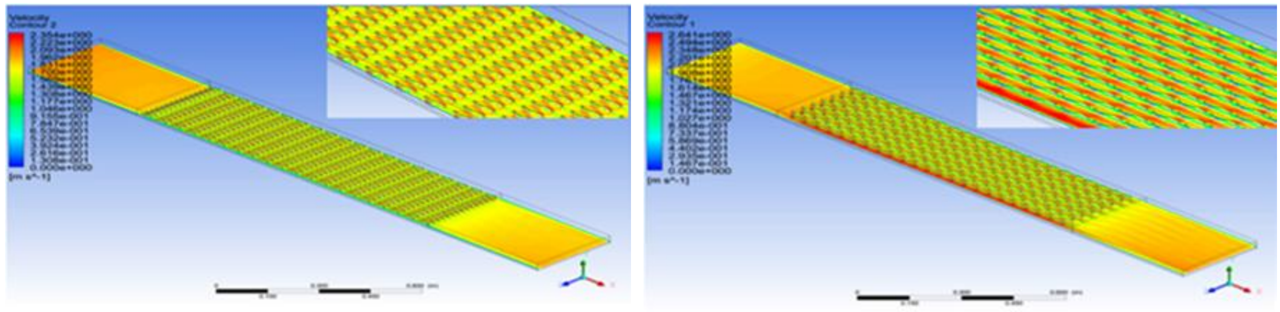

a **b**

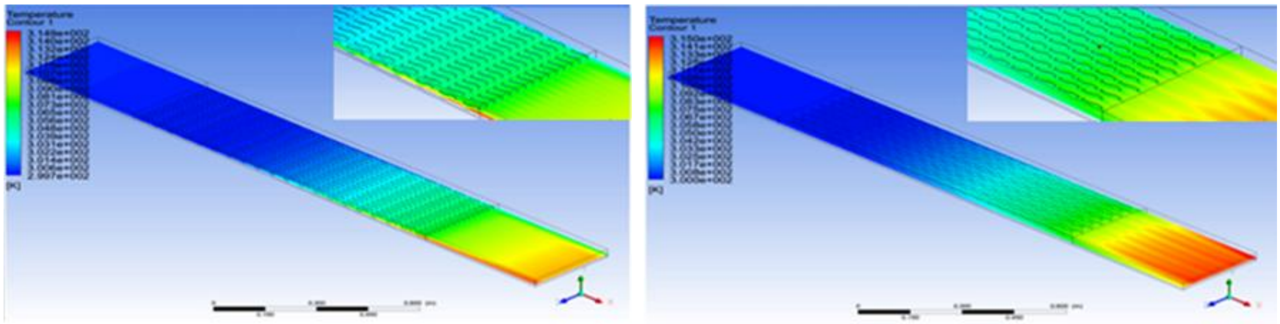

c **d**

Figure 7. Temperature & velocity distributions for airflow along the SP-SAH for the same v=2 m/s, and at *p/H*=1.667 and l/H=0.8335: (a) inline S-shaped velocity, (b) staggered S-shaped velocity (c) inline S-shaped temp. (d) Staggered S-shaped temp.

5.2 The impact of the relative roughness of a pitch

Figure 8 demonstrates the velocity contours at various *p/H* values. At a velocity of v = 1.5 m/s and a Re = 5545, the figures show that velocity distribution is affected by the use of artificial roughness, and that pitch also has an effect on velocity distribution.

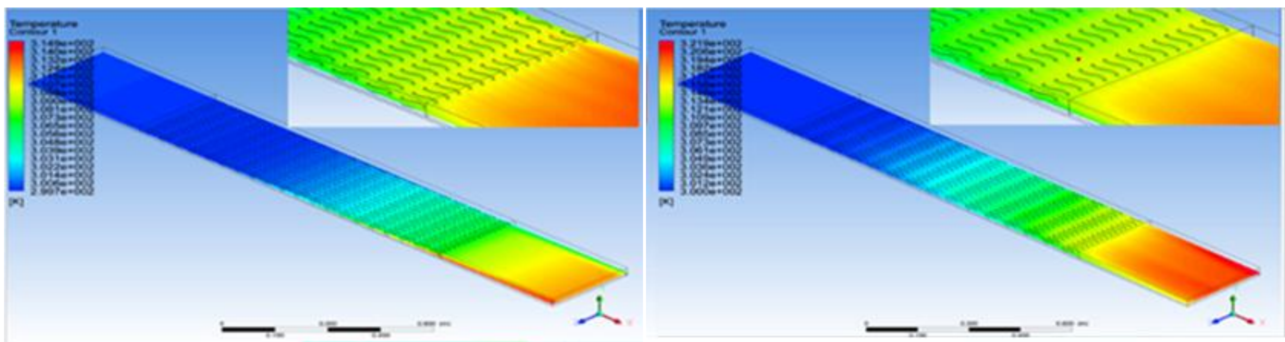

a **b**

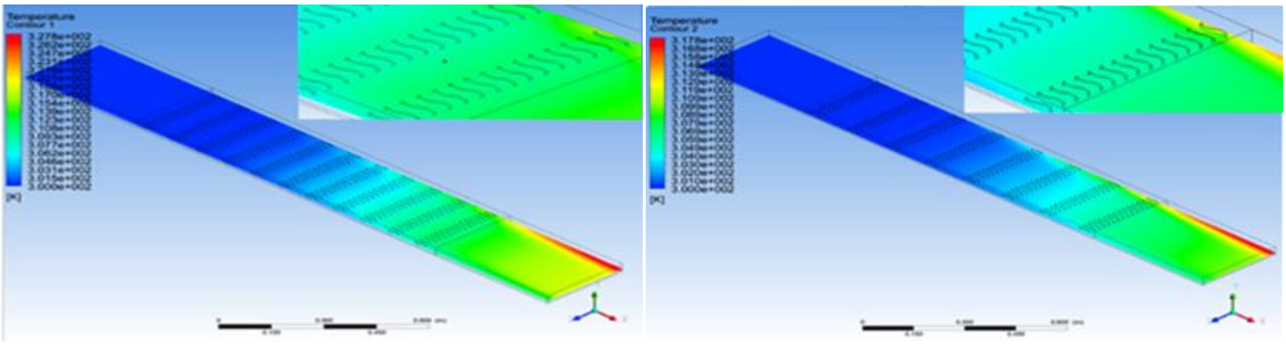

c d

Figure 8. Velocity contours for airflow along the SP-SAH at v=1.5 m/s with inline and S-shapes at (a) *p/H*=1.667, (b)*p/H*=3.33 (c) *p/H*=5. (d) *p/H*=6.667

Figures 9a and 9b show the temperature contours along a SAH with artificial roughness in an S-shape for inline and staggered arrangements, respectively, with varying pitch values. In the case of S-shaped artificial roughness, the temperatures of *p/H* and l/H are observed to be higher and farther from the absorber, as indicated by the contours. The temperature contours indicate that the staggered S-shape has a maximum temperature of 327 K, while the inline S-shape has a maximum temperature of 324 K. This also suggests less air mixing and turbulence, resulting in a larger variance in air temperature for the S-shaped inline configuration compared to the staggered configuration.

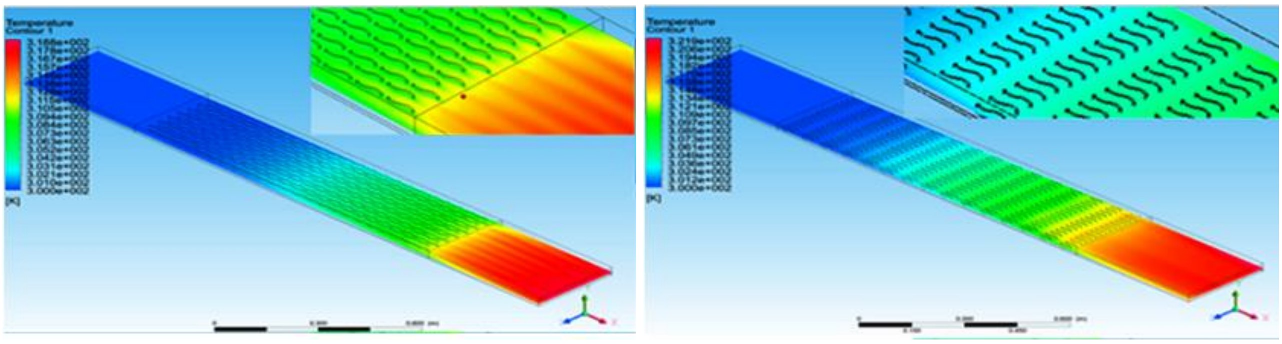

a b

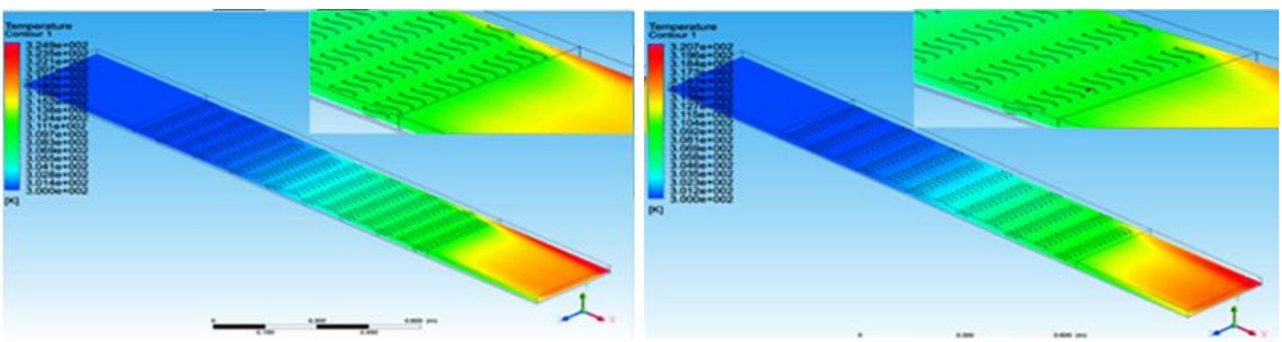

c d

Figure 9. temperature contours for airflow along the SP-SAH for the same v=1.5 m/s inline S-shapes : (a) *p/H*=1.667, (b) *p/H*=3.33 (c) *p/H*=5 ,(d) *p/H*=6.667

This study aims to examine the influence of pitch (p/H) on the Nusselt number of both arrangements. Figure 10 illustrates the relationship between the Nusselt number (Nu) and the dimensionless parameter (p/H). It is observed that Nu grows as (p/H) increases, reaching a peak value at (p/H=10), beyond which it subsequently falls. This is due to the optimal mixing of fluid at this value and efficient HT from the surface.

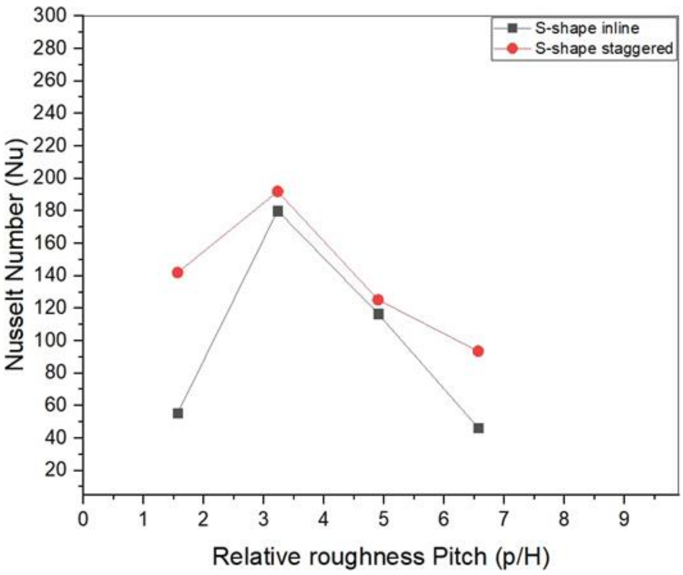

Figure 10. Deviation of *Nu* concerning relative *p/H* with fixed Re=5545.

5.3 The impact of Reynolds number on heat transfer

Figures 11a and 11b depict the relationship between the p/H parameter and the Nu and f variables, as well as (l/H) variable, respectively. The plots illustrate the relationship between the Nusselt number (Nu) and the friction factor (f) as a function of the Reynolds number (Re), while keeping the other roughness parameters at constant values. Figures 11a and 11b show that both the *Nu* and *f* reach their maximum values at a *p/H* of 3.33 and a relative roughness length (l/H) of 1.667. Notably, these values significantly decrease on both sides of this pitch and length pair. The formation of the boundary layer is observed to occur upstream of the subsequent rib following the reattachment of the free shearing layer downstream of the rib. These processes are responsible for the observed variation. At lower *p/H* ratios, these phenomena are not as pronounced. Moreover, when the pitch value exceeds 3.33, there is a decrease in the quantity of reattachment sites along the surface of the heat transfer absorber plate. Nonetheless, the distance between the reattachment point and the upstream rib has a generally consistent value. Consequently, when the *p/H* value increases beyond 3.33 but remains below 1.667, the heat transfer rate declines.

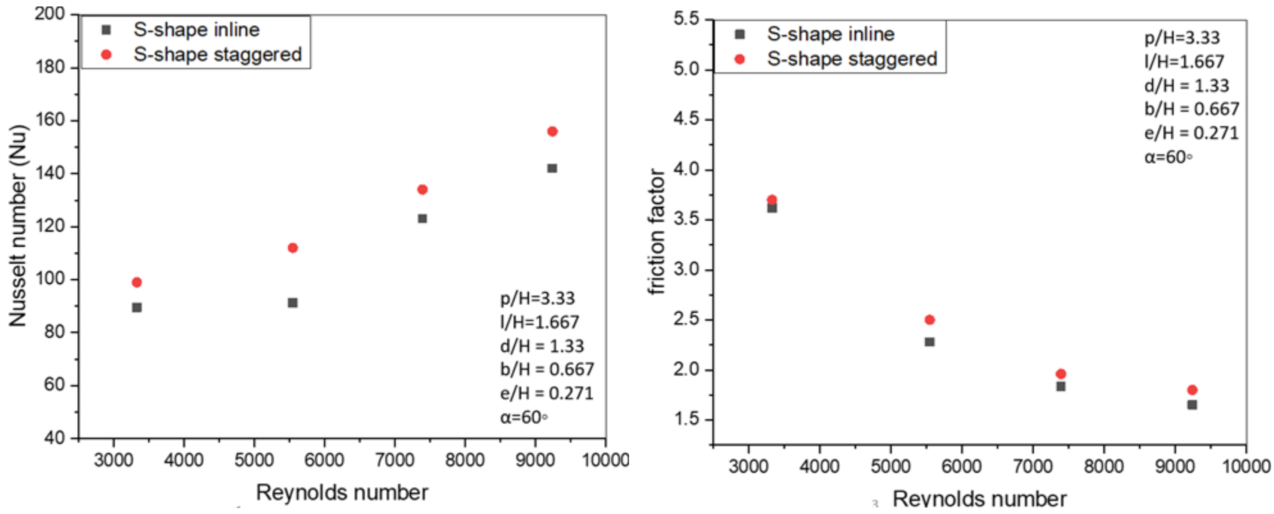

a b

Figure 11. (a) *Nu* Variation regarding Re for *p/H*=3.33 and l/H=1.667. (b) *f* Variation regarding the Re for *p/H*=3.33 and l/H=1.667

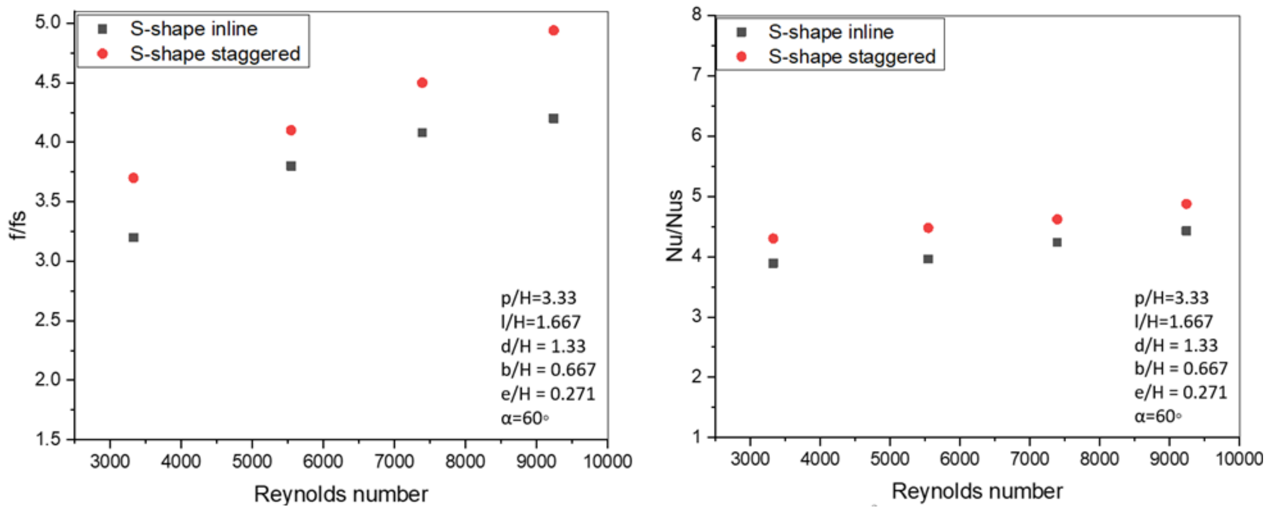

a b

Figure 12. (a) f/fs ratio Variation with Re for *p/H*=3.33 and l/H=1.667. (b) *Nu* ratio Variation with the Re for *p/H*=3.33 and l/H=1.667.

5.4 Nusselt number

The investigation focused on enhancing HT using S-shaped ribs with both inline and staggered arrangements on the AP. The influence was assessed by numerical and experimental methods. Figures 13 and 14 reveal that the *Nu* increases with the introduction of obstacles in the gas flow, as depicted in the figures. For both arrangements, the *Nu* initially increases with the rise in *p/H* and length scale (l/H) but gradually decreases beyond certain values, as observed in Figures 13 and 14. The maximum *Nu* occurs when the relative roughness length (l/H) is 1.667 for staggered arrangements. Nevertheless, it was discovered that there was a marginal drop in the Nusselt number as the pH value went from 3.33 to 6.667, and the length scale (l/H) increased from 1.667 to 3.33. The changes in the *Nu* are attributed to the impact of clearance on airflow velocity through the gap and the fluctuating turbulence areas. As the air flows over the S-shaped rib, turbulence is generated, promoting heat transfer downstream. However, the flow velocity of air through the S-shaped rib decreases with increasing *p/H* and length scales (l/H). Consequently, the disrupted area of air decreases, leading to reduced HT effects. Moreover, for staggered S-shaped ribs, the *Nu* increased when the ratio of rib length to channel height (l/H) was 1.667, likely because of fluid reattachment downstream of the rib. The number of reattachment sites increased as the ratios of *p/H* and l/H rose, resulting in an increase in heat transfer. Figures 17 and 18 demonstrate a consistent ratio of the *Nu* to other parameters for both inline and staggered arrangements. Clearly, the *Nu* decreases with increasing pitch (*p/H*) of the surface roughness regarding a given relative roughness length (e/H). This decrease can be attributed to the reduced number of attachment locations on the AP as the *p/H* increases. The S-shaped configuration generates secondary currents, leading to better turbulent mixing and heat transfer, contributing to an increase in the *Nu*.

5.5 Friction Factor

Figures 15 and 16 present the f variation concerning the *p/H* for an inline S-shape and (l/H) for a staggered S-shape. As the Re rises, the laminar sub-layer gets suppressed, leading to a complete emergence of turbulent flow in the duct, confirming the prediction and resulting in a decrease in the f. The observed trend indicates that, for a specific value of relative roughness height (e/H), the friction factor (f) reduces as the ratio of pitch to hydraulic diameter (p/H) grows for the inline S-shape, and as the p/H ratio increases for the staggered S-shape. The decline in f can be ascribed to a decrease in the quantity of obstructions inside the channel of flow. The graphic in Figures 19 and 20 displays the f ratio as a function of *p/H* and l/H, while keeping (d/H = 1.33), (e/H = 0.271), and (b/H = 0.667) constant for various Reynolds numbers. As the Reynolds numbers grow, the ratio of friction factors falls with an increase in relative roughness pitch. This trend is observed at L/H = 3.33 for the staggered arrangement and p/H = 6.667 for the inline design. In conclusion, an increase in pitch roughness reduces heat conduction and increases friction.

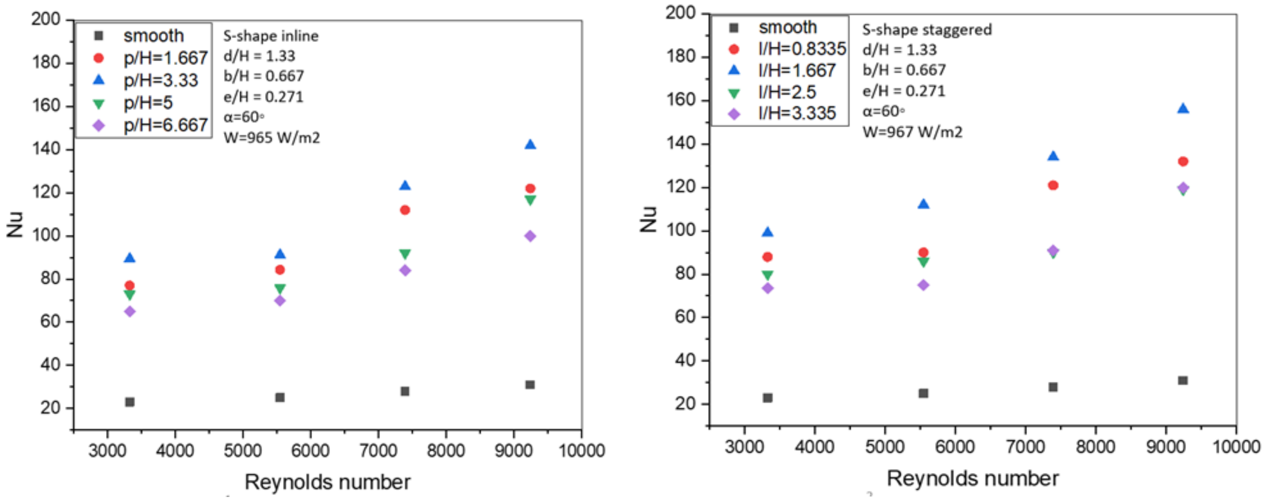

a b

Figure 13. ***Nu*** **variation with respect to Re for (a) staggered S-shape and (b) inline S-shape configurations.**

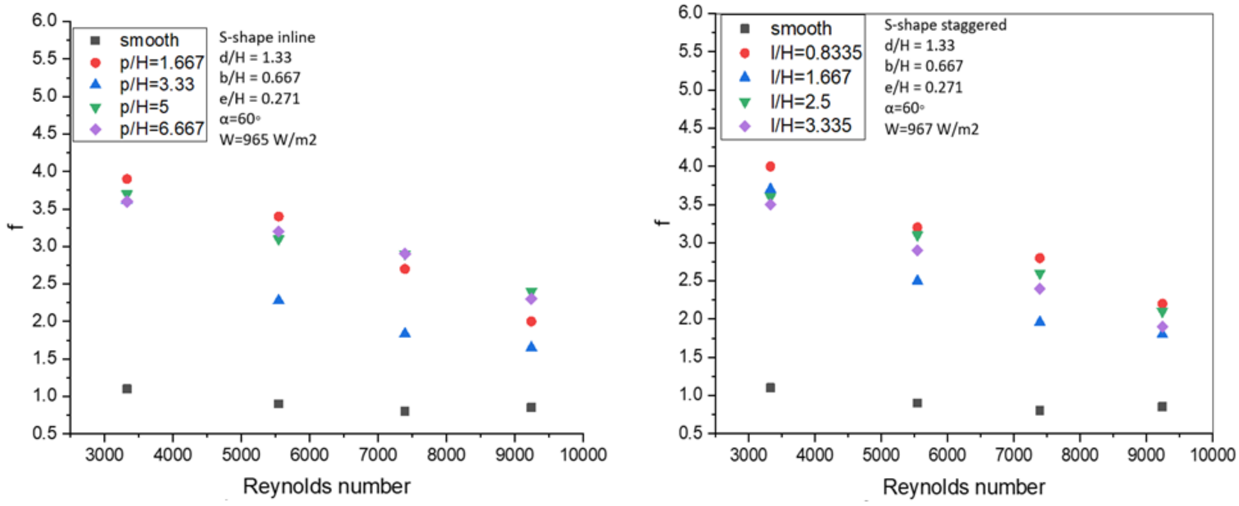

a b

Figure 14. ***f*** **variation with respect to Re for (a) inline S-shape and (b) staggered S-shape.**

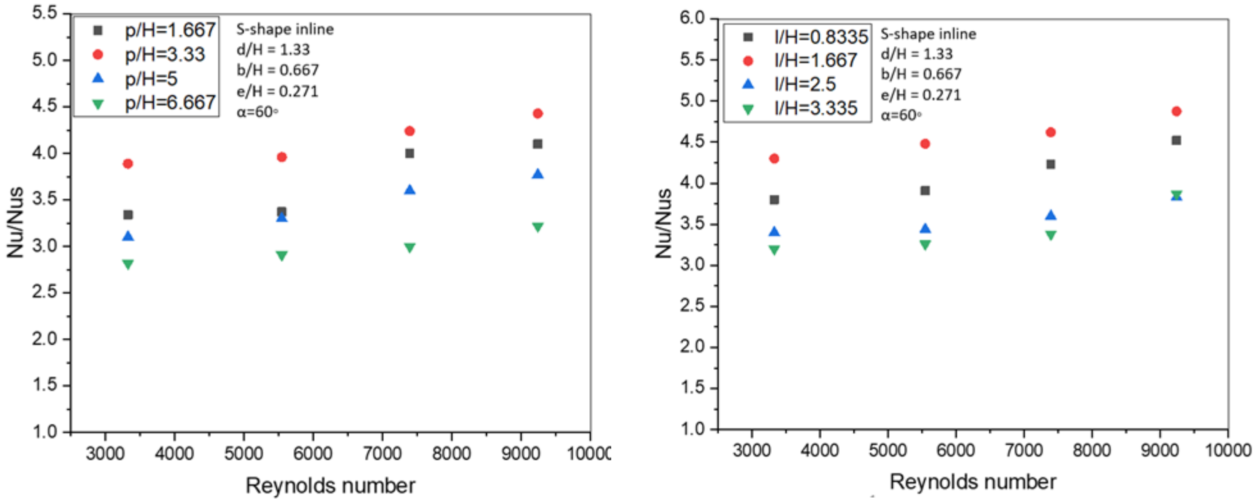

a **b**

Figure 15. Effect of (a) *p/H* (b) l/H on *Nu* ratio.

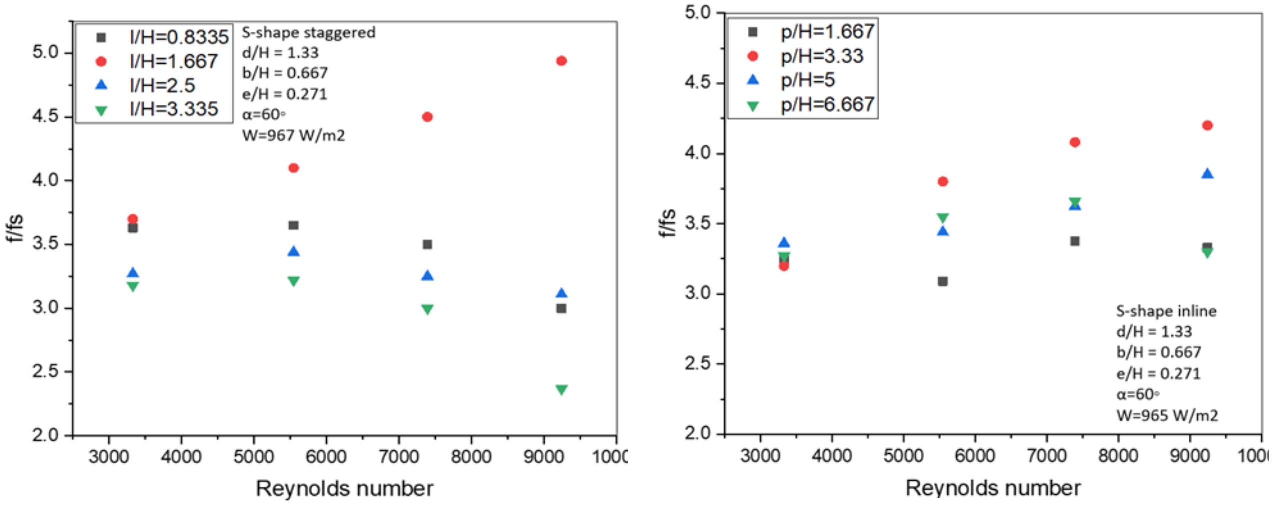

a **b**

Figure 16. Effect of (a) 1/H (b) *p/H* on *f* ratio.

5.6 Effect of *p/H* and l/H on TPF

The artificially roughened duct's HT and flow friction properties have been investigated, and the results show that when HT improves, friction power improves as well because of an increase in the *f*. The findings from the current experimental and numerical investigation provide confirmation that, at a Reynolds number (Re) of 9241, the duct with roughened surfaces, characterized by a pitch-to-height ratio (p/H) of 1.667, and with fixed values of diameter-to-height ratio (d/H) of 1.33, expansion-to-height ratio (e/H) of 0.271, and contraction-to-height ratio (b/H) of 0.667, along with an inclination angle (α) of 60 degrees, exhibits an average Nusselt number (Nu) that is approximately 4.875 times higher than that of the smooth duct. Furthermore, a recent study conducted by Kumar

Sahu et al. in 2022 focused on investigating curved geometries. The peak thermal performance of the SAH was seen at a certain relative roughness height (e/D) of 0.0454, roughness pitch (P/e) of 8, and an angle of attack (α) of 60°. In comparison to the conventional smooth annular passage, the annular passage with a roughened apex upstream, known as SAH, demonstrated noteworthy enhancements. Specifically, the SAH configuration resulted in a 2.83 increase in the Normalized Nu Enhancement Ratio (NNER) and a 1.50 increase in the f Enhancement Ratio (FFER) throughout the various design and operating circumstances investigated. The maximal thermo-hydraulic improvement parameter (THIP) was calculated to be 157.49%. The statistical correlation between the f and Nu variables has been examined in relation to the low parameter of the surface with arc-shaped apex upstream and roughness geometry in the context of SAH [6]. The experimental work conducted by Singh Patel et al. and referenced in the text reveals that the highest rise in the Nusselt number is observed at a ratio of protrusion height (p) to hydraulic diameter (H) of 10. Additionally, the maximum increase in the friction factor is recorded at a p/H ratio of 8, in comparison to a uniform surface [44]. The thermo-hydraulic performance parameter (THPP) achieves its optimal value when the pH is 10 and the Reynolds number is 12,364. Correlations have been established to quantify the relationship between thermal transfer and the f parameter for the SAH duct. The mathematical model utilized for the design and performance prediction of SAH ducts under various operating situations has been validated through the utilization of experimental data. The parameter provided by (Eq.12) allows for the simultaneous evaluation of thermal-hydraulic performance. Parameters with values greater than one indicate that using an enhancement device is effective, and they may be used to evaluate several configurations and determine which one is best. Figure 21 displays a comprehensive comparison of the effects of l/H and *p/H* on TPF. In all cases, as depicted in Figure 21, the thermal enhancement factor fluctuates based on the Reynolds number. The thermal enhancement factors ranged from 1.8 to 3.5 for all parameters tested. This study examines the impact of the rib height to channel height ratio (l/H) and the pitch to channel height ratio (p/H) on the thermal performance factor (TPF). Ducts with a staggered rectangular S-shape design, featuring roughness elements spaced 1.2 cm apart (e) and a pitch of 15 cm (i.e., l/H = 1.667), exhibit excellent thermal enhancement with a factor of 3.13 for the range of Reynolds numbers studied. To validate the computational fluid dynamics (CFD) model, a comparison is made between the RFSAH model without baffle parameters and the RFSAH model without porous material parameters.

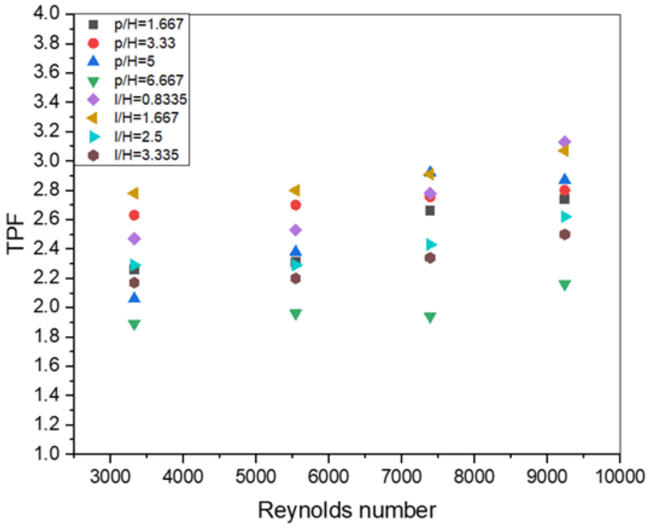

Figure 21. A Comparative Analysis of the Engineering and Thermal Efficiency of Different Models.

The introduction of S-shaped ribs in the design increases the occurrence of crossflows in the spanwise direction. The induction of turbulence at numerous sites is facilitated by the integration of openings in geometries characterized by continuous shapes, hence enhancing the mixing of main and secondary flows. The heat transfer coefficient for spherical and inclined rib protrusions is notably enhanced due to the altered flow pattern in the vicinity of the roughened surface. The increased blending of primary and secondary flows occurring at the trailing edge of the inclined rib can be attributed to two key factors: the existence of a highly turbulent three-dimensional wake caused by the spherical protrusion, and the creation of secondary flow over the rib. These mechanisms work together to promote increased mixing in that specific region. The enhanced level of mixing observed in this context is a contributing factor to the elevated rate of heat transfer within the system of interest, specifically the SAH [44]. The presence of vortices near the rib contributes to a significantly higher HT rate in an AP with trapezoidal winglets alone. Incorporating trapezoidal winglets with undulating grooves in the SAH not only enhances the HT rate compared to previous designs but also reduces pressure loss to a significant extent. The incorporation of channels in conjunction with triangular, undulating ribs serves to disturb the recirculation zone that forms behind the ribs, resulting in a more significant enhancement of the heat transfer coefficient [30]. The observed distinct gaps in the roughness sections enhance the intensity of mixing between the secondary vortex flow and the primary flow, resulting in an increased heat transfer rate. The presence of surface roughness, characterized by discrete multi-V-rib and staggered rib structures, promotes improved heat transfer throughout the system [5] was found to have the highest mean *Nu*, whereas ducts with chamfered ribs and triangular grooves [23,45]. Among the studied range of parameters, ribs combined with staggered elements were found to exhibit the lowest mean *Nu* when compared to ribs with a curved shape [44].

6. Conclusions and Future Outlook

The study involved conducting experiments and doing three-dimensional computational fluid dynamics analysis to examine the heat transfer and fluid flow characteristics within a rectangular duct of a solar air heater with one wall that had been roughened. The roughened wall featured a rectangular S-shape in two configurations: staggered and inline. The thermal performance of the roughness geometry is a critical factor, where the orientation and cross-section of the irregularity hold significant relevance. The presence of ribs oriented perpendicular to the primary flow direction led in the formation of stagnant vortices behind the rib. This phenomenon caused localized zones of elevated temperature and a reduction in the heat transfer rate. Angled ribs with a gap reduced the intensity of the cross flow and failed to energize the principal flow stream, resulting in a lower HT rate at the leading edges. Circular cross-section ribs created larger eddy dimensions (recirculation zones) behind them than other cross-section ribs (chamfered, wedge, square, triangular), leading to an observable decrease in the HT rate. Despite their popularity due to accessibility and operability, circular cross-section ribs exhibited such limitations. To mitigate the recirculation zone effect, transverse ribs were combined with perforations. However, creating channels on the AP physically presented challenges.

The impact of the Reynolds number, roughness pitch, relative roughness pitch, and relative roughness length has been examined, revealing their influence on the heat transfer coefficient and the friction factor, respectively. The current experimental findings have been compared to numerical results obtained under flow conditions that are similar to those found in the experiments. Experimental and computational fluid dynamics (CFD) research has focused on flows with medium Reynolds numbers (Re = 3,000 to 10,000). A comparison between the *Nu* and the *f* for an artificial roughness that is staggered and shaped like a S is shown here. It was discovered that the greatest rise in the *Nu* takes place when the parameter values are (l/H = 1,667), (d/H = 1.33), and (e/H = 0.271), and it was also discovered that the highest *f* takes place at the same parameter. The maximum estimated thermo-hydraulic performance factor is 3.13, suggesting that the utilization of S-shaped roughness elements results in superior performance. The following are the principal conclusions derived from the present experimental work:

- Each hybrid roughness appears to have an optimal parameter configuration for maximising heat transfer while minimising friction coefficient and Reynolds number increase.
- Staggered elements contribute to increased heat transfer by promoting flow reattachment, flow dispersal, and the formation of a wake behind the staggered ribs. Additionally, the

larger openings in the rib lead to increased flow turbulence as the flow accelerates through them. These combined effects result in improved heat transfer. Several experimental investigations have been undertaken to enhance performance by introducing complex roughness on the airfoil surface. However, the utilization of numerical and computational fluid dynamics methods is considered a developing domain in this particular sector.

- Due to the computational complexity, few studies have addressed the mathematical calculation of the roughness of curved ribs, and with proper validation, CFD can be implemented as a low-cost, quick, and effective calculation method. This procedure can determine the optimal design and number of ribs for solar heaters. Therefore, more research is required in this field.

REFERENCES

[1] M.E. Shayan, G. Najafi, B. Ghobadian, S. Gorjian, R. Mamat, M.F. Ghazali, Multi-microgrid optimization and energy management under boost voltage converter with Markov prediction chain and dynamic decision algorithm, Renew. Energy. 201 (2022) 179–189. https://doi.org/10.1016/J.RENENE.2022.11.006.

[2] S. Chaurasia, V. Goel, A. Debbarma, Impact of hybrid roughness geometry on heat transfer augmentation in solar air heater: A review, Sol. Energy. (2023). https://doi.org/10.1016/J.SOLENER.2023.02.052.

[3] S. Abbas, Y. Yuan, A. Hassan, J. Zhou, W. Ji, T. Yu, U.U. Rehman, S. Yousuf, Design a low-cost, medium-scale, flat plate solar air heater: An experimental and simulation study, J. Energy Storage. 56 (2022) 105858. https://doi.org/10.1016/J.EST.2022.105858.

[4] V.B. Gawande, A.S. Dhoble, D.B. Zodpe, CFD analysis to study effect of circular vortex generator placed in inlet section to investigate heat transfer aspects of solar air heater, Sci. World J. 2014 (2014).

[5] A.S. Kashyap, R. Kumar, P. Singh, V. Goel, Solar air heater having multiple V-ribs with Multiple-Symmetric gaps as roughness elements on Absorber-Plate: A parametric study, Sustain. Energy Technol. Assessments. 48 (2021) 101559. https://doi.org/10.1016/J.SETA.2021.101559.

[6] M.K. Sahu, M. Kharub, M.M. Matheswaran, Nusselt number and friction factor correlation development for arc-shape apex upstream artificial roughness in solar air heater, Environ. Sci. Pollut. Res. 29 (2022) 65025–65042. https://doi.org/10.1007/S11356-022-20222-0/TABLES/9.

[7] A.S. Yadav, M.K. Dwivedi, A. Sharma, V.K. Chouksey, CFD based heat transfer correlation for ribbed solar air heater, Mater. Today Proc. 62 (2022) 1402–1407.

https://doi.org/10.1016/J.MATPR.2021.12.382.

[8] A.F. Sharol, A.A. Razak, Z.A.A. Majid, M.A.A. Azmi, M.A.S.M. Tarminzi, Y.H. Ming, Z.A. Zakaria, M.A. Harun, A. Fazlizan, K. Sopian, Effect of thermal energy storage material on the performance of double-pass solar air heater with cross-matrix absorber, J. Energy Storage. 51 (2022) 104494. https://doi.org/10.1016/J.EST.2022.104494.

[9] B. Brahma, A.K. Shukla, D.C. Baruah, Design and performance analysis of solar air heater with phase change materials, J. Energy Storage. 61 (2023) 106809. https://doi.org/10.1016/J.EST.2023.106809.

[10] S. Sharma, R.K. Das, K. Kulkarni, Performance evaluation of solar air heater using sine wave shape obstacle, in: Curr. Adv. Mech. Eng., Springer, 2021: pp. 541–553.

[11] A.A. Elbrashy, F.S. Abou-Taleb, M.K. El-Fakharany, F.A. Essa, Experimental study of solar air heater performance by evacuated tubes connected in series and loaded with thermal storage material, J. Energy Storage. 54 (2022) 105266. https://doi.org/10.1016/J.EST.2022.105266.

[12] M.K. Sahu, R.K. Prasad, Exergy based performance evaluation of solar air heater with arc-shaped wire roughened absorber plate, Renew. Energy. 96 (2016) 233–243. https://doi.org/10.1016/J.RENENE.2016.04.083.

[13] M.K. Sahu, R.K. Prasad, Thermohydraulic performance analysis of an arc shape wire roughened solar air heater, Renew. Energy. 108 (2017) 598–614. https://doi.org/10.1016/J.RENENE.2017.02.075.

[14] M. Abuşka, Energy and exergy analysis of solar air heater having new design absorber plate with conical surface, Appl. Therm. Eng. 131 (2018) 115–124. https://doi.org/https://doi.org/10.1016/j.applthermaleng.2017.11.129.

[15] O.R. Alomar, H.M. Abd, M.M. Mohamed Salih, Efficiency enhancement of solar air heater collector by modifying jet impingement with v-corrugated absorber plate, J. Energy Storage. 55 (2022) 105535. https://doi.org/10.1016/J.EST.2022.105535.

[16] A.P. Singh, Varun, Siddhartha, Heat transfer and friction factor correlations for multiple arc shape roughness elements on the absorber plate used in solar air heaters, Exp. Therm. Fluid Sci. 54 (2014) 117–126. https://doi.org/https://doi.org/10.1016/j.expthermflusci.2014.02.004.

[17] A.K. Patil, J.S. Saini, K. Kumar, Experimental investigation of enhanced heat transfer and pressure drop in a solar air heater duct with discretized broken V-rib roughness, J. Sol. Energy Eng. 137 (2015) 21013.

[18] N.P. Nwosu, Employing exergy-optimized pin fins in the design of an absorber in a solar air heater, Energy. 35 (2010) 571–575. https://doi.org/https://doi.org/10.1016/j.energy.2009.10.027.

[19] B.S. Qader, E.E. Supeni, M.K.A. Ariffin, A.R.A. Talib, Numerical investigation of flow through inclined fins under the absorber plate of solar air heater, Renew. Energy. 141 (2019) 468–481.

https://doi.org/https://doi.org/10.1016/j.renene.2019.04.024.

[20] J.J. Fiuk, K. Dutkowski, Experimental investigations on thermal efficiency of a prototype passive solar air collector with wavelike baffles, Sol. Energy. 188 (2019) 495–506. https://doi.org/https://doi.org/10.1016/j.solener.2019.06.030.

[21] A.J. Mahmood, Experimental Study of a Solar Air Heater With a New Arrangement of Transverse Longitudinal Baffles, J. Sol. Energy Eng. 139 (2017). https://doi.org/10.1115/1.4035756.

[22] R. Maithani, S. Chamoli, A. Kumar, A. Gupta, Solar air heater duct roughened with wavy delta winglets: correlations development and parametric optimization, Heat Mass Transf. 55 (2019) 3473–3491.

[23] A. Kumar, A. Layek, Nusselt number and friction factor correlation of solar air heater having winglet type vortex generator over absorber plate, Sol. Energy. 205 (2020) 334–348. https://doi.org/https://doi.org/10.1016/j.solener.2020.05.047.

[24] G. Madhulatha, M. Mohan Jagadeesh Kumar, P. Sateesh, Optimization of tube arrangement and phase change material for enhanced performance of solar air heater- A numerical analysis, J. Energy Storage. 41 (2021) 102876. https://doi.org/10.1016/J.EST.2021.102876.

[25] D. Chaatouf, A.G. Ghiaus, S. Amraqui, Optimization of a solar air heater using a phase change material for drying applications, J. Energy Storage. 55 (2022) 105513. https://doi.org/10.1016/J.EST.2022.105513.

[26] R. Kumar, V. Goel, P. Singh, A. Saxena, A.S. Kashyap, A. Rai, Performance evaluation and optimization of solar assisted air heater with discrete multiple arc shaped ribs, J. Energy Storage. 26 (2019) 100978. https://doi.org/10.1016/J.EST.2019.100978.

[27] A.K. Singh, N. Agarwal, A. Saxena, Effect of extended geometry filled with and without phase change material on the thermal performance of solar air heater, J. Energy Storage. 39 (2021) 102627. https://doi.org/10.1016/J.EST.2021.102627.

[28] S.S. Patel, A. Lanjewar, Heat transfer enhancement using additional gap in symmetrical element of V-geometry roughened solar air heater, J. Energy Storage. 38 (2021) 102545. https://doi.org/10.1016/J.EST.2021.102545.

[29] F. Chabane, N. Moummi, S. Benramache, Experimental study of heat transfer and thermal performance with longitudinal fins of solar air heater, J. Adv. Res. 5 (2014) 183–192.

[30] A. Saxena, N. Agarwal, E. Cuce, Thermal performance evaluation of a solar air heater integrated with helical tubes carrying phase change material, J. Energy Storage. 30 (2020) 101406. https://doi.org/10.1016/J.EST.2020.101406.

[31] S. Singh, P. Dhiman, Analytical and experimental investigations of packed bed solar air heaters under the collective effect of recycle ratio and fractional mass flow rate, J. Energy Storage. 16 (2018) 167–

186. https://doi.org/10.1016/J.EST.2018.01.003.

[32] P. Raturi, H. Deolal, S. Kimothi, Numerical analysis of the return flow solar air heater (RF-SAH) with assimilation of V-type artificial roughness, Energy Built Environ. (2022). https://doi.org/10.1016/J.ENBENV.2022.09.002.

[33] J.P. Hartnett, W.M. Rohsenow, Handbook of heat transfer, Handb. Heat Transf. (1973).

[34] S. Skullong, S. Kwankaomeng, C. Thianpong, P. Promvonge, Thermal performance of turbulent flow in a solar air heater channel with rib-groove turbulators, Int. Commun. Heat Mass Transf. 50 (2014) 34–43.

[35] Varun, R.P. Saini, S.K. Singal, Investigation of thermal performance of solar air heater having roughness elements as a combination of inclined and transverse ribs on the absorber plate, Renew. Energy. 33 (2008) 1398–1405. https://doi.org/https://doi.org/10.1016/j.renene.2007.07.013.

[36] H. Benli, Experimentally derived efficiency and exergy analysis of a new solar air heater having different surface shapes, Renew. Energy. 50 (2013) 58–67. https://doi.org/https://doi.org/10.1016/j.renene.2012.06.022.

[37] H.K. Ghritlahre, R.K. Prasad, Prediction of exergetic efficiency of arc shaped wire roughened solar air heater using ANN model, Int. J. Heat Technol. 36 (2018) 1107–1115.

[38] R.L. Webb, Performance evaluation criteria for use of enhanced heat transfer surfaces in heat exchanger design, Int. J. Heat Mass Transf. 24 (1981) 715–726.

[39] T.L. Bergman, T.L. Bergman, F.P. Incropera, D.P. Dewitt, A.S. Lavine, Fundamentals of heat and mass transfer, John Wiley & Sons, 2011.

[40] C.K.G. Lam, K. Bremhorst, A Modified Form of the k-ε Model for Predicting Wall Turbulence, J. Fluids Eng. 103 (1981) 456–460. https://doi.org/10.1115/1.3240815.

[41] D.C. Wilcox, Reassessment of the scale-determining equation for advanced turbulence models, AIAA J. 26 (1988) 1299–1310.

[42] H.K. Versteeg, W. Malalasekera, An introduction to computational fluid dynamics: the finite volume method, Pearson education, 2007.

[43] F.P. Incropera, D.P. Dewitt, T.L. Bergman, A.S. Lavine, Introduction to Heat Transfer, John Wiley&Sons, Inc. United States Am. (1996) 280–284.

[44] S. Singh Patel, A. Lanjewar, Experimental and numerical investigation of solar air heater with novel V-rib geometry, J. Energy Storage. 21 (2019) 750–764. https://doi.org/10.1016/J.EST.2019.01.016.

[45] L. Joshi, D. Choudhary, P. Kumar, J. Venkateswaran, C.S. Solanki, Does involvement of local community ensure sustained energy access? A critical review of a solar PV technology intervention in rural India, World Dev. 122 (2019) 272–281. https://doi.org/10.1016/j.worlddev.2019.05.028.